Monthly Notices of the ROYAL ASTRONOMICAL SOCIETY

MNRAS **515,** 6093–6108 (2022)
Advance Access publication 2022 July 29

https://doi.org/10.1093/mnras/stac2118

Chemical abundance of LINER galaxies – metallicity calibrations based on SDSS-IV MaNGA

C. B. Oliveira, Jr [1]★ A. C. Krabbe [1]★ J. A. Hernandez-Jimenez [1] O. L. Dors, Jr [1] I. A. Zinchenko,[2,3] G. F. Hägele,[4,5] M. V. Cardaci [4,5] and A. F. Monteiro[1,6]

[1] *Universidade do Vale do Paraíba, Av. Shishima Hifumi 2911, São José dos Campos, SP 12244-000, Brazil*
[2] *Faculty of Physics, Ludwig-Maximilians-Universität, Scheinerstr. 1, D-81679 Munich, Germany*
[3] *Main Astronomical Observatory, National Academy of Sciences of Ukraine, 27 Akad. Zabolotnoho St., UA-03680 Kyiv, Ukraine*
[4] *Instituto de Astrofísica de La Plata (CONICET La Plata–UNLP), Avenida Centenario, Paseo del Bosque, S/N, B1900FWA, La Plata, Argentina*
[5] *Facultad de Ciencias Astronómicas y Geofísicas, Universidad Nacional de La Plata, Paseo del Bosque s/n, 1900 La Plata, Argentina*
[6] *Instituto Federal do Maranhão, Av. Newton Bello, s/n, Imperatriz, MA 65906-335, Brazil*

Accepted 2022 July 20. Received 2022 June 24; in original form 2022 March 11

ABSTRACT

The ionizing source of low-ionization nuclear emission-line regions (LINERs) is uncertain. Because of this, an empirical relation to determine the chemical abundances of these objects has not been proposed. In this work, for the first time, we derived two semi-empirical calibrations based on photoionization models to estimate the oxygen abundance of LINERS as a function of the *N*2 and *O*3*N*2 emission-line intensity ratios. These relations were calibrated using oxygen abundance estimations obtained by comparing the observational emission-line ratios of 43 LINER galaxies (taken from the MaNGA survey) and grids of photoionization models built with the CLOUDY code assuming post-asymptotic giant branch stars with different temperatures. We found that the oxygen abundance of LINERs in our sample is in the $8.48 \lesssim 12 + \log(\mathrm{O/H}) \lesssim 8.84$ range, with a mean value of $12 + \log(\mathrm{O/H}) = 8.65$. We recommend the use of the *N*2 index to estimate the oxygen abundances of LINERs, since the calibration with this index presented a much smaller dispersion than the *O*3*N*2 index. In addition, the estimated metallicities are in good agreement with those derived by extrapolating the disc oxygen abundance gradients to the centre of the galaxies showing that the assumptions of the models are suitable for LINERs. We also obtained a calibration between the logarithm of the ionization parameter and the [O III]/[O II] emission-line ratio.

Key words: ISM: abundances – galaxies: abundances – galaxies: nuclei.

1 INTRODUCTION

Chemical abundance is a fundamental parameter for understanding the formation and evolution of galaxies. The metallicity (*Z*), i.e. the content of metals relative to hydrogen, is usually traced and parametrized by the oxygen abundance relative to the hydrogen (O/H) of the gas phase, since oxygen is one of the most abundant elements produced after primordial nucleosynthesis. The metallicity of the gas phase of star-forming regions (SFs) and active galactic nuclei (AGNs) can mainly be estimated using two methods. The first method, called T_e method, is based on direct determinations of electron temperatures (for a review, see Peimbert, Peimbert & Delgado-Inglada 2017 and Pérez-Montero 2017) and requires measurements of auroral emission lines such as [O III] λ4363 and [N II] λ5755, which are generally weak or not measurable in objects with high metallicity or low excitation (van Zee et al. 1998; Díaz et al. 2007; Dors et al. 2008). This technique is used to derive the gas-phase metallicity in SFs and is widely accepted as producing the most reliable oxygen abundance estimates (Pilyugin 2003; Hägele et al. 2006, 2008; Toribio San Cipriano et al. 2017). The second method is used when it is not possible to measure the auroral lines and the T_e method cannot be applied. Known as the strong-line method or indirect method, as suggested by Pagel et al. (1979), who followed the original idea of Jensen, Strom & Strom (1976), this method is based on calibrations between the oxygen abundance (or metallicity) and strong emission lines easily measured in SF region spectra (for a review, see López-Sánchez & Esteban 2010, Maiolino & Mannucci 2019, and Kewley, Nicholls & Sutherland 2019).

For oxygen abundances in AGNs, narrow-line regions (NLRs) of Seyfert 2 are by far the most studied, using both the T_e method (Alloin et al. 1992; Izotov & Thuan 2008; Dors et al. 2015, 2020) and strong-line methods (e.g. Storchi-Bergmann et al. 1998; Castro et al. 2017; Carvalho et al. 2020). On the other hand, for low-ionization nuclear emission-line regions (LINERs), chemical abundance studies are rarely found in the literature. LINERs appear in 1/3 of galaxies in the local Universe (Netzer 2013), and their ionization sources are still an open problem in astronomy. Heckman (1980) suggested that the main ionization/heating source of these nuclei is gas shocks. Later, Halpern & Steiner (1983) and Ferland & Netzer (1983) proposed that the accretion gas in a central black hole (AGN) should be responsible for the ionization of LINERs. Thus, the difference between LINERs and other AGN types would consist in the order of magnitude of the ionization parameter

★ E-mail: cbo_jr@hotmail.com (CBO); angela.krabbe@gmail.com (ACK)

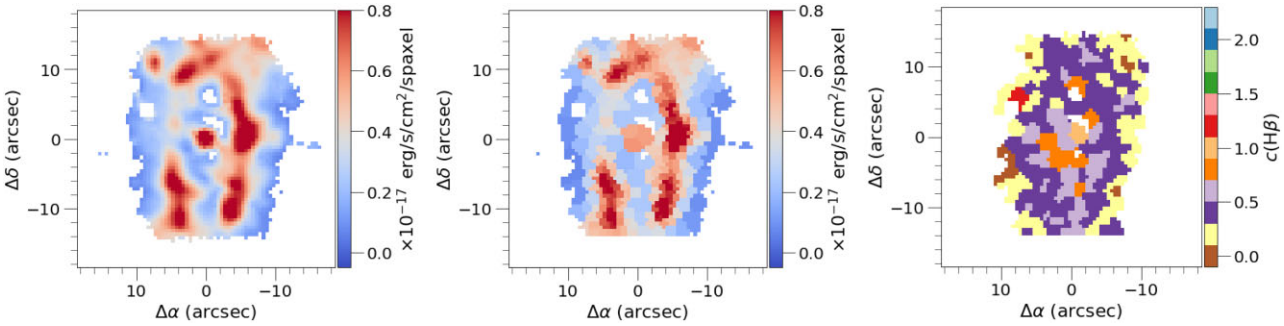

Figure 1. Example of the tessellation binning based on the Hβ S/N map for 8313-12705. Left-hand panel: Hβ emission-line flux map. Centre panel: Voronoi re-binned Hβ emission-line flux map. Right-hand panel: derived reddening map.

(Ho, Filippenko & Sargent 1993). However, Terlevich & Melnick (1985) and Shields (1992) proposed that the LINER-like emission is produced by photoionization due to hot stars that came out of the main sequence (e.g. in the post-asymptotic giant branch, post-AGB). Based on this scenario, Taniguchi, Shioya & Murayama (2000) showed that photoionization models, considering planetary nebula nuclei with a temperature of 10^5 K as ionizing sources, can reproduce the region occupied, at least, for a subset of type 2 LINERs in optical emission-line ratio diagnostic diagrams. Others authors (Yan & Blanton 2012, Singh et al. 2013, and Bremer et al. 2013) also proposed that these objects have composite ionizing sources, and more than one mechanism could be responsible for the gas ionization.

The unknown nature of the ionizing sources and excitation mechanisms of LINERs make it difficult to determine their metallicity using the T_e method and/or strong-line methods. Storchi-Bergmann et al. (1998) found that their calibrations work very well for the Seyfert galaxies, yielding abundance values that agree with those obtained from the extrapolation of O/H abundance gradients to the central regions of the host galaxies. However, for the LINERs, their calibrations yield lower values (up to ∼0.5 dex) than those derived through the extrapolation of O/H abundance gradients, and they concluded that their model assumptions were not suitable for LINERs. Regarding the T_e-method application to LINERs, Yan (2018) determined the electron temperature in the S^+ and O^+ zones for a sample of quiescent red sequence galaxies with low-ionization regions using spectra from the Sloan Digital Sky Survey (SDSS) and compared the temperature-sensitive line ratios with different model predictions to infer the metallicity of these galaxies. They found that neither the photoionization models simulated pure AGN nor the shock models simultaneously reproduced all studied line ratios. For example, high temperatures estimated from [S II] and [N II] line ratios imply subsolar metallicities, while their [N II]/[O II] line ratios required supersolar metallicities. In a recent work, Krabbe et al. (2021) estimated the oxygen abundance of the LINER nucleus of the UGC 4805 galaxy through the extrapolation of the radial abundance gradient, as well as strong emission-line calibrations for AGNs and photoionization models assuming gas accretion into a black hole (representing an AGN) and post-AGB stars with different temperatures. These authors found that all O/H abundance estimations agreed with each other. Although both AGN and post-AGB models were able to reproduce the observational data, the high gas excitation level that must be maintained at kpc scales and the results from the $\log(EW_{H\alpha})$ versus log([NII]λ6584) diagnostic diagram (WHAN) diagram suggest that the main ionizing source of the UGC 4805 nucleus probably has a stellar origin rather than an AGN.

In this paper, we propose two new metallicity abundance calibrations for LINERS by using $N2 = \log$ ([N II] λ6584/Hα) and $O3N2 = \log\left(\frac{[\text{O III}]\,\lambda5007/\text{H}\beta}{[\text{N II}]\,\lambda6583/\text{H}\alpha}\right)$ strong emission-line indices. To calibrate the new relations, we combined observational data with photoionization models assuming post-AGB stars as ionizing sources. Our sample is composed of 43 galaxies with LINER emission in their nuclear region and with SF emission in their discs. The observational data were compiled from the Mapping Nearby Galaxies at APO (MaNGA; Bundy et al. 2015) survey. This paper is organized as follows: Section 2 describes the observational data and the selection criteria of the sample. The methodology used to obtain the metallicity calibrations is presented in Section 3. Section 4 contains the results obtained, which are discussed in Section 5. The conclusion of the outcome is provided in Section 6.

2 OBSERVATIONAL DATA

2.1 MaNGA overview and measurements

MaNGA is an integral field spectroscopy (IFS) survey[1] (Bundy et al. 2015), which observed about 10 000 galaxies in the local Universe. This survey is part of the Sloan Digital Sky Survey (SDSS-IV; Blanton et al. 2017) and was performed using a 2.5 m telescope at the Apache Point Observatory. The spectra have a wavelength coverage of 3600–10 300 Å, with a spectral resolution of $R \sim 1400$ at $\lambda \sim 4000$ Å and $R \sim 2600$ at $\lambda \sim 9000$ Å, with a spatial resolution of about 2.5 arcsec due to the mean local seeing (Smee et al. 2013; Drory et al. 2015; Wake et al. 2017).

MaNGA applies a data analysis pipeline[2] (DAP) on the reduced IFS cubes to produce two-dimensional (2D) physical property maps (Belfiore et al. 2019; Westfall et al. 2019). Here, we describe, briefly, the DAP procedure. First, it performs a Voronoi re-binning of the cubes based on a g-band weighted signal-to-noise ratio (S/N) image to reach an S/N of at least 10 on each target. Secondly, on the cube binned, the DAP fits the stellar continuum by using the Penalized PiXel-Fitting (pPXF) method by Cappellari (2017). The stellar templates are built by hierarchically clustering the MILES stellar library (Sánchez-Blázquez et al. 2006; Falcón-Barroso et al. 2011). Finally, after the stellar continuum fitting continuum-subtracted spectra (the 'nebular' ones), the DAP computes measurements of the emission-line fluxes in two ways: one based on simple moments and another based on a Gaussian fitting. For further details, we refer

[1] https://www.sdss.org/surveys/manga/
[2] https://www.sdss.org/dr15/manga/manga-analysis-pipeline/

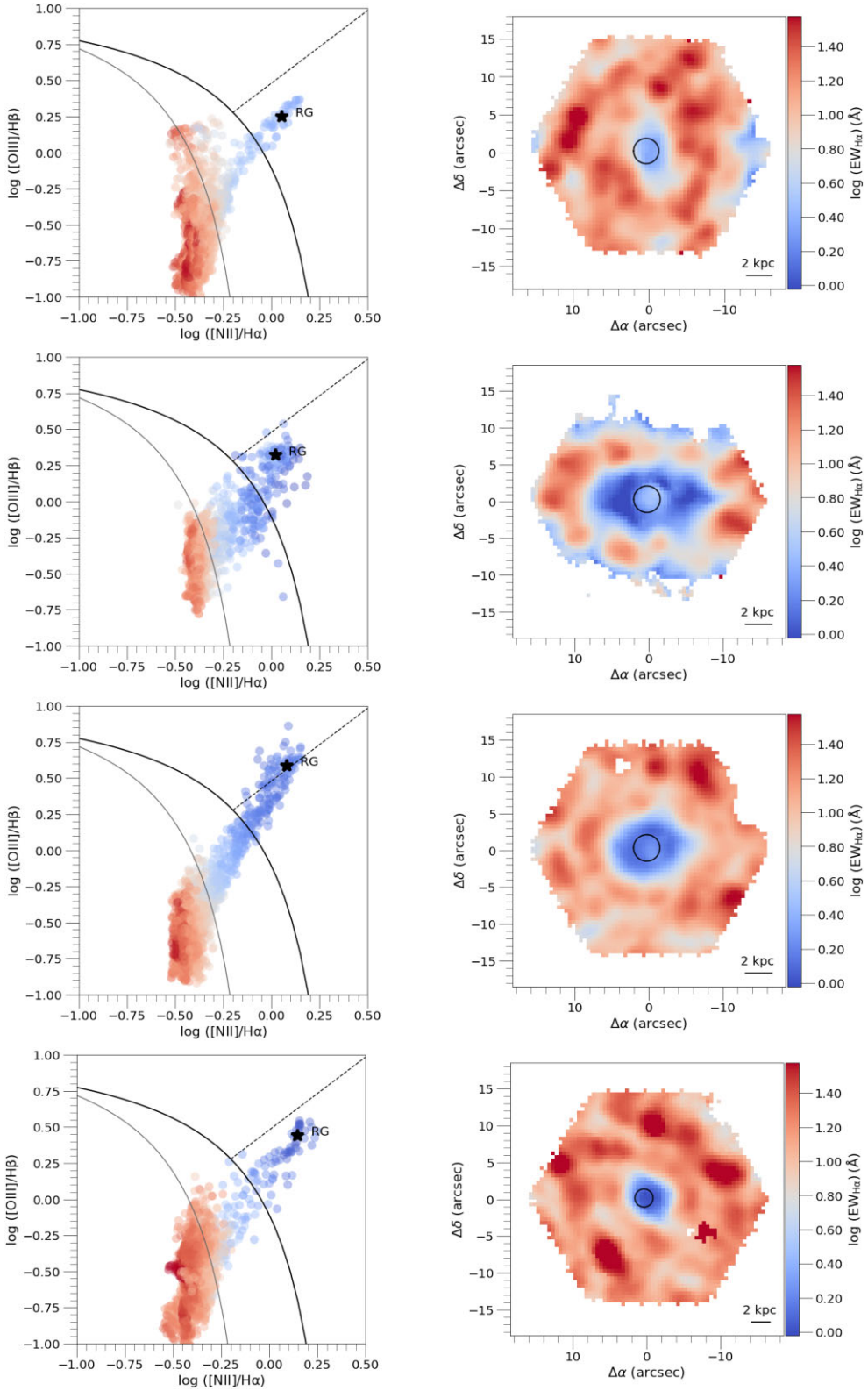

Figure 2. First column: log([O III] λ5007/Hβ) versus log([N II] λ6584/Hα) diagnostic diagram; from top to bottom, the galaxies shown are 7495-12704, 7990-12704, 8249-12704, and 8318-12703. The black solid curve represents the theoretical upper limit for the SFs proposed by Kewley et al. (2001) (Ke01); the grey solid curve is the empirical star-forming limit proposed by Kauffmann et al. (2003) (Ka03); and the black dashed line represents the separation between Seyferts and LINERs (Cid Fernandes et al. 2010). The region between the Ke01 and Ka03 lines is a denominated composite region. Point colours are the same as in the second column and depend on the EW$_{H\alpha}$. Second column: spatial distribution according to the log(EW$_{H\alpha}$). The black stars represent the integrated estimations for the nuclear regions defined by the black circles.

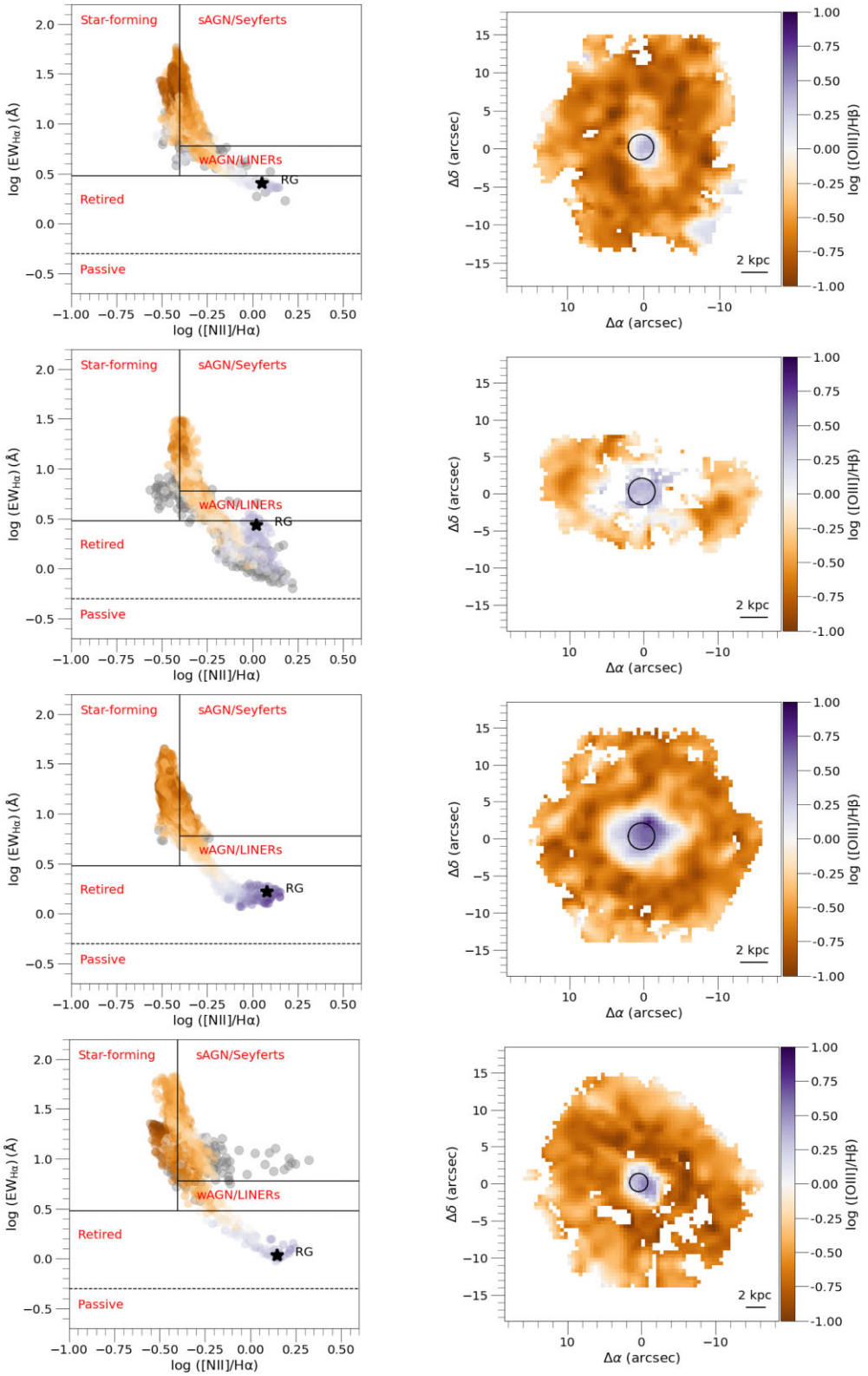

Figure 3. First column: examples of WHAN diagrams; from top to bottom, the galaxies are 7495-12704, 7990-12704, 8249-12704, and 8318-12703. Point colours are the same as in the second column and depend on the log([O III]/Hα) ratio. Second column: spatial distribution according to the log([O III]/Hα) ratio. The black stars represent the integrated estimations for the nuclear regions defined by the black circles.

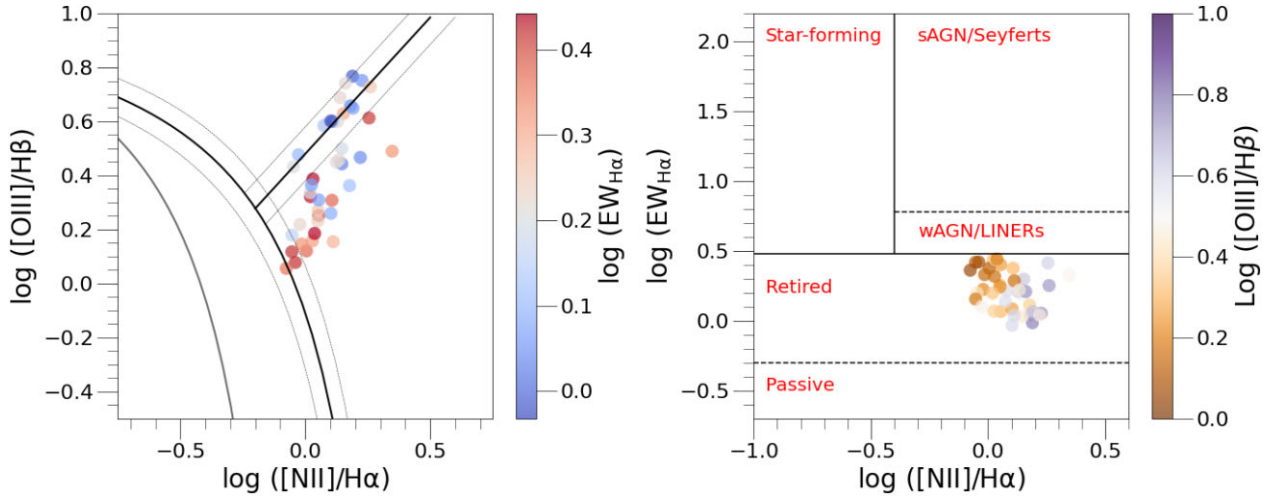

Figure 4. BPT and WHAN diagrams as shown in Figs 2 and 3 but considering the nuclear integrated flux for each galaxy in our sample.

the reader to Belfiore et al. (2019) and Westfall et al. (2019). For this work, we use the 2D maps built using the Gaussian fitting set taken from the Data Release 15 of MaNGA[3] (Aguado et al. 2019).

To work with reliable data, we masked all spaxels with S/N <3 in the 2D emission-line fluxes and equivalent width maps. All emission-line intensities were reddening corrected using the extinction curve by Cardelli, Clayton & Mathis (1989). The theoretical value used for the Hα/Hβ ratio is 2.87, which was obtained for the recombination case B for an electron temperature of 10 000 K at the limit of the low density (Osterbrock & Ferland 2006). We derived the 2D reddening coefficient [c(Hβ)] maps re-binning by S/N the Hβ image using the publicly available Voronoi binning algorithm by Cappellari & Copin (2003). The target S/N per tessellation bin was 30. Fig. 1 is an example of Hβ flux and c(Hβ) tessellated maps for the galaxy 8313-12705.

2.2 Sample selection

As mentioned in Krabbe et al. (2021), we selected objects with LINER emission in their nuclear regions and SF emission in their discs. Furthermore, this sample is restricted to objects with LINER emission with an integrated Hα equivalent width (EW$_{H\alpha}$) lower than 3 and higher than 0.5, which suggests that the ionization source of the nuclear region is probably post-AGBs. The sample selection followed the steps listed below.

(i) We used the log([O III] λ5007/Hβ) versus log([N II] λ6584/Hα) diagnostic diagram proposed by Baldwin, Phillips & Terlevich (1981), called BPT, to classify objects as H II-like regions, composite, and AGN-like objects considering the theoretical and empirical criteria proposed by Kewley et al. (2001) and Kauffmann et al. (2003), respectively. The Seyfert and LINER objects are distinguished using the Kewley et al. (2006) criteria.

(ii) We used the log(EW$_{H\alpha}$) versus log([N II] λ6584/Hα) diagnostic diagram, known as WHAN (Cid Fernandes et al. 2011), to verify if the nuclear regions initially classified as LINER using the BPT diagram occupy the same area as in the WHAN diagram. The WHAN diagram is useful to differentiate the nature of the ionization sources of LINERs, i.e. between evolved low-mass stars (like post-AGB stars) and low-ionization AGNs. Using the EW$_{H\alpha}$, this diagram classifies objects into five classes of galaxies, namely:

(a) Pure star-forming galaxies: log([N II]/Hα) $<$ $-$0.4 and EW$_{H\alpha}$ $>$ 3 Å.
(b) Strong AGNs: log([N II]/Hα) $>$ $-$0.4 and EW$_{H\alpha}$ $>$ 6 Å.
(c) Weak AGNs: log([N II]/Hα) $>$ $-$0.4 and EW$_{H\alpha}$ between 3 and 6 Å.
(d) Retired galaxies (RGs; i.e. fake AGNs): EW$_{H\alpha}$ $<$ 3 Å.
(e) Passive galaxies (actually, lineless galaxies): EW$_{H\alpha}$ and EW$_{[N II]}$ $<$ 0.5 Å.

From the BPT and WHAN diagrams together with their spatial distributions, we selected all objects whose nuclei are in the LINER zone in the first diagram and the RG zone in the second. We also required that the disc spaxels be in the SF zone of both diagrams. The BPT and WHAN diagrams are in Figs 2 and 3, respectively, together with their spatial distributions, for the galaxies 7495-12704, 7990-12704, 8249-12704, and 8318-12703 belonging to our final sample. At this step, we selected all objects with the same spatial distribution pattern, following the procedures below.

(iii) A circular aperture with a radius of 1 kpc was defined for each galaxy selected earlier. The integrated flux for each emission line considered was obtained for all nuclei in our sample by summing together all fluxes in this region. The BPT and WHAN diagrams were repeated for the nuclear regions of the galaxies and are shown in Fig. 4. We also include in this figure, as a black star, the nuclear integrated line ratios in the corresponding diagrams for each object, as shown in Figs 2 and 3. Finally, we selected all objects whose integrated nuclear emission is located in the LINER and RG zones in the BPT and WHAN diagrams, respectively. For the BPT diagram (Fig. 4), deviations of 0.1 dex were considered for the lines that represent the separation between Seyferts/LINERs and AGNs-like/SFs. These variations were assumed because according to Kewley et al. (2001), the lines separating the different regions have errors of the order of 0.1 dex, which are from the modelling due to the assumptions made in the chemical abundances, chemical depletion factors, slope of the initial mass function, and stellar atmosphere models (Kewley et al. 2001).

[3]https://www.sdss.org/dr15/

Table 1. Identification number of the plate, coordinates, redshift (z), distance (Mpc), and logarithm of the integrated stellar mass in units of solar masses ($M_\odot$).

Plate-IFU	RA (deg)	Dec. (deg)	Redshift	Distance (Mpc)	log (M_*) ($M_\odot$)
7495-12704	205.4384	27.0048	0.0292	125.29	10.72
7977-3704	332.7987	11.8007	0.0272	116.48	10.36
7977-12703	333.2018	13.3341	0.0744	330.60	11.00
7990-6103	261.2849	58.7647	0.0296	125.33	10.32
7990-12704	262.4861	58.3974	0.0271	116.46	10.51
8083-12704	50.6968	0.1494	0.0231	98.90	10.44
8131-9102	112.2214	41.3078	0.0586	256.17	9.97
8140-12703	117.8985	42.8801	0.0323	138.58	10.83
8243-9102	130.8217	52.7579	0.0591	260.66	11.10
8243-12701	128.6877	52.7157	0.0452	196.78	11.16
8247-3701	136.6714	41.3651	0.0252	107.68	10.35
8249-12704	137.3775	45.9524	0.0271	116.46	10.67
8252-12702	145.5309	48.1549	0.0339	143.10	10.88
8254-3704	164.0822	43.7549	0.0362	156.36	10.76
8257-1902	166.2978	46.1029	0.0371	160.81	10.64
8258-12704	167.7765	43.6330	0.0253	107.68	10.79
8259-9102	178.5399	44.3661	0.0620	274.51	10.99
8313-9102	239.9880	41.4778	0.0335	143.05	10.72
8313-12705	242.6825	41.1486	0.0319	134.22	10.91
8318-12703	196.2324	47.5036	0.0396	169.85	10.99
8320-9102	206.8303	21.8338	0.0527	228.69	11.02
8332-12705	209.2520	43.3620	0.0333	143.03	10.93
8330-9102	205.0114	40.4209	0.0245	103.31	10.45
8332-6103	207.6574	43.7641	0.0489	210.51	10.58
8440-12704	136.1423	41.3978	0.0274	116.49	10.54
8481-1902	237.6539	53.3906	0.0654	288.53	10.77
8482-12703	245.5031	49.5208	0.0500	215.07	10.96
8549-3703	241.4164	46.8466	0.0575	251.55	10.67
8550-6103	247.6387	39.8307	0.0249	103.36	10.41
8550-12704	247.0584	40.3138	0.0334	143.04	10.72
8550-12705	249.1357	39.0279	0.0303	129.72	11.04
8552-9101	226.9119	44.5563	0.0664	293.17	10.86
8601-12705	250.1231	39.2351	0.0300	129.68	10.47
8588-9101	250.1562	39.2216	0.0355	151.95	10.63
8138-3702	116.0979	44.5277	0.0500	215.07	10.72
8138-9101	117.3026	45.5103	0.0535	233.21	10.84
8482-3704	245.4124	49.4488	0.0328	138.65	10.86
8482-9101	241.7996	48.5726	0.0437	187.85	10.84
8554-1902	183.1133	35.8835	0.0231	98.90	10.02
8603-12703	247.2827	40.6650	0.0303	129.71	10.49
8604-12703	247.7642	39.8385	0.0309	129.79	10.79
8604-6102	246.0735	39.2110	0.0303	129.72	10.68
8606-3702	253.7939	36.9063	0.0239	98.97	10.30

The final sample consists of 43 galaxies with a LINER-type nucleus. The stellar mass of the hosting galaxies is in the range of $9.97 \lesssim \log(M_*/M_\odot) \lesssim 11.16$ and the redshift is in the range of $0.02 \lesssim z \lesssim 0.07$. For each galaxy of our sample, Table 1 lists the identification number of the plate, coordinates, redshift, distance, and integrated stellar mass. All information was taken from the manga.Pipe3D[4] and manga.drpall[5] (see Sánchez et al. 2016). Fig. 5 shows SDSS images combining the *gri* bands of the galaxies 7495-12704, 7990-12704, 8249-12704, and 8318-12703 together with the MaNGA field of view and the 2D maps of the spatial distribution of Hα flux. In Table 2, the reddening-corrected emission-line intensities,

[4]https://data.sdss.org/datamodel/files/MANGA_PIPE3D
[5]https://data.sdss.org/datamodel/files/MANGA_SPECTRO_REDUX

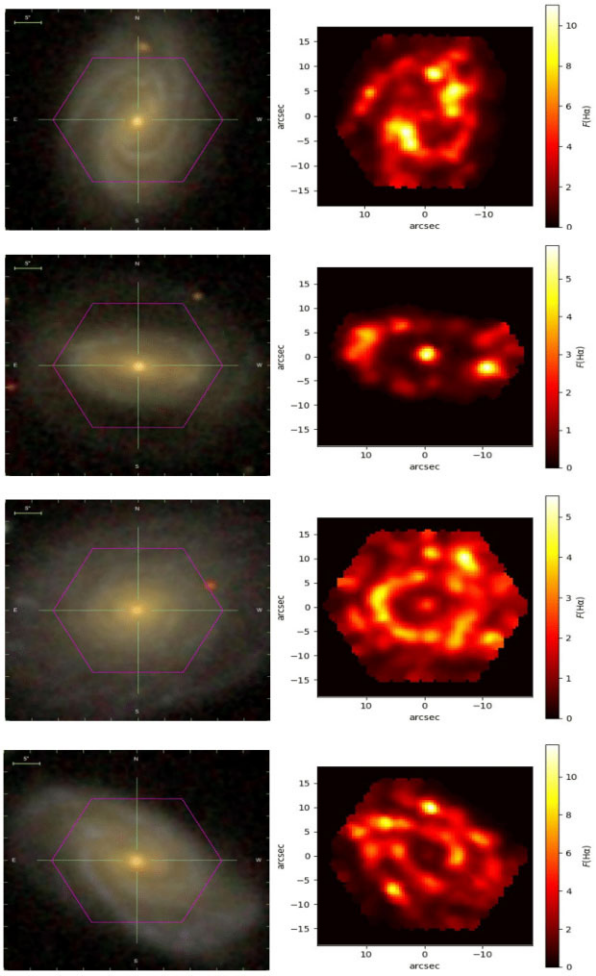

Figure 5. Left-hand panels: SDSS image combining the *gri* bands of galaxies 7495-12704, 7990-12704, 8249-12704, and 8318-12703 (from top to bottom) with the MaNGA field of view indicated by the purple hexagon. Right-hand panels: Hα flux spatial distribution (in units of 10^{-17} erg cm^{-2} spaxel^{-1}).

the reddening coefficient [$c(\mathrm{H}\beta)$], and the equivalent widths of Hα for each LINER nucleus are listed.

3 METHODS

This section describes the methodology used to derive two new oxygen abundance calibrations for LINERS by using the *N*2 and *O3N*2 indices. To calibrate the new relations, we combined observational data with photoionization models assuming post-AGB stars as ionizing sources. In Section 3.1, we present the photoionization models used to derive oxygen abundances and ionization parameter values for the integrated fluxes from the central regions of the galaxies, and in Section 3.2, we discuss an indirect method, the determination of the nuclear oxygen abundances by extrapolating the metallicity gradients obtained through H II region estimations, and we compare them with those derived using the new calibrations.

3.1 Photoionization models

We built photoionization model grids using the version 17.00 of the CLOUDY code (Ferland et al. 2017). Post-AGB stars were considered as the ionization sources since the nuclei of the objects in our sample have been classified as RGs according to the WHAN diagnostic

Table 2. Reddening-corrected emission-line intensities (in relation to Hβ = 1.00) were derived for each LINER nucleus in our sample. Values of the $EW_{H\alpha}$ and the reddening coefficient [$c(H\beta)$] are also listed.

Plate-IFU	[O II] λ3727	Hβ	[O III] λ5007	Hα	[N II] λ6584	$EW_{H\alpha}$	$c(H\beta)$
7495-12704	1.77 ± 0.03	1.00 ± 0.01	1.79 ± 0.01	2.87 ± 0.01	3.25 ± 0.01	2.52 ± 0.05	0.36
7977-3704	5.06 ± 0.09	1.00 ± 0.02	1.65 ± 0.02	2.87 ± 0.01	2.73 ± 0.02	1.68 ± 0.04	0.40
7977-12703	3.93 ± 0.24	1.00 ± 0.06	1.31 ± 0.06	2.87 ± 0.03	2.54 ± 0.03	2.62 ± 0.08	0.31
7990-6103	11.40 ± 0.30	1.00 ± 0.04	2.71 ± 0.05	2.87 ± 0.02	2.57 ± 0.01	1.58 ± 0.07	0.24
7990-12704	4.35 ± 0.04	1.00 ± 0.01	2.10 ± 0.01	2.87 ± 0.01	3.01 ± 0.01	2.72 ± 0.06	0.28
8083-12704	2.27 ± 0.03	1.00 ± 0.01	1.32 ± 0.01	2.87 ± 0.01	2.90 ± 0.01	2.38 ± 0.06	0.26
8131-9102	25.56 ± 0.91	1.00 ± 0.09	4.55 ± 0.12	2.87 ± 0.04	4.35 ± 0.01	1.09 ± 0.05	0.33
8140-12703	8.77 ± 0.18	1.00 ± 0.02	1.87 ± 0.03	2.87 ± 0.01	3.23 ± 0.01	1.79 ± 0.04	0.41
8243-9102	10.61 ± 0.35	1.00 ± 0.04	3.09 ± 0.04	2.87 ± 0.02	6.39 ± 0.01	2.12 ± 0.04	0.54
8243-12701	12.46 ± 0.30	1.00 ± 0.04	4.26 ± 0.05	2.87 ± 0.02	4.08 ± 0.02	1.99 ± 0.05	0.52
8247-3701	3.58 ± 0.03	1.00 ± 0.01	1.44 ± 0.01	2.87 ± 0.01	3.06 ± 0.01	2.08 ± 0.03	0.29
8249-12704	4.25 ± 0.06	1.00 ± 0.02	3.88 ± 0.02	2.87 ± 0.01	3.45 ± 0.01	1.64 ± 0.04	0.34
8252-12702	27.75 ± 0.53	1.00 ± 0.06	5.86 ± 0.06	2.87 ± 0.02	4.44 ± 0.01	0.97 ± 0.03	0.40
8254-3704	5.62 ± 0.21	1.00 ± 0.04	2.04 ± 0.05	2.87 ± 0.03	3.25 ± 0.02	1.17 ± 0.05	0.55
8257-1902	3.90 ± 0.06	1.00 ± 0.01	1.40 ± 0.02	2.87 ± 0.01	2.77 ± 0.01	2.14 ± 0.03	0.45
8258-12704	35.74 ± 0.38	1.00 ± 0.04	5.64 ± 0.04	2.87 ± 0.01	4.84 ± 0.01	1.13 ± 0.04	0.26
8259-9102	8.45 ± 0.29	1.00 ± 0.05	2.44 ± 0.06	2.87 ± 0.02	3.08 ± 0.02	2.74 ± 0.06	0.42
8313-9102	5.05 ± 0.11	1.00 ± 0.03	2.30 ± 0.03	2.87 ± 0.02	4.32 ± 0.02	1.30 ± 0.05	0.31
8313-12705	5.55 ± 0.09	1.00 ± 0.02	3.16 ± 0.03	2.87 ± 0.02	4.02 ± 0.02	1.53 ± 0.05	0.38
8318-12703	4.19 ± 0.14	1.00 ± 0.04	2.77 ± 0.05	2.87 ± 0.03	4.02 ± 0.04	1.07 ± 0.05	0.40
8320-9102	4.70 ± 0.16	1.00 ± 0.04	2.81 ± 0.05	2.87 ± 0.03	3.82 ± 0.03	1.63 ± 0.06	0.36
8332-12705	18.37 ± 0.35	1.00 ± 0.04	4.46 ± 0.05	2.87 ± 0.02	4.46 ± 0.01	1.16 ± 0.03	0.47
8330-9102	2.29 ± 0.07	1.00 ± 0.03	1.82 ± 0.03	2.87 ± 0.02	3.63 ± 0.03	1.22 ± 0.06	0.48
8332-6103	7.97 ± 0.31	1.00 ± 0.06	3.84 ± 0.07	2.87 ± 0.04	3.40 ± 0.03	1.38 ± 0.07	0.29
8440-12704	3.82 ± 0.04	1.00 ± 0.01	1.71 ± 0.01	2.87 ± 0.01	3.23 ± 0.01	1.74 ± 0.04	0.23
8481-1902	6.57 ± 0.28	1.00 ± 0.08	2.17 ± 0.09	2.87 ± 0.05	3.00 ± 0.05	1.58 ± 0.06	0.55
8482-12703	10.04 ± 0.24	1.00 ± 0.05	4.10 ± 0.05	2.87 ± 0.03	5.17 ± 0.03	2.59 ± 0.10	0.30
8549-3703	16.61 ± 0.41	1.00 ± 0.07	4.88 ± 0.09	2.87 ± 0.04	3.96 ± 0.04	1.67 ± 0.06	0.32
8550-6103	4.73 ± 0.04	1.00 ± 0.01	1.53 ± 0.01	2.87 ± 0.01	3.13 ± 0.01	2.77 ± 0.05	0.38
8550-12704	10.91 ± 0.21	1.00 ± 0.05	2.93 ± 0.04	2.87 ± 0.02	4.77 ± 0.02	1.10 ± 0.05	0.31
8550-12705	9.88 ± 0.24	1.00 ± 0.04	3.98 ± 0.04	2.87 ± 0.02	3.71 ± 0.02	1.10 ± 0.04	0.68
8552-9101	6.49 ± 0.22	1.00 ± 0.05	1.43 ± 0.06	2.87 ± 0.03	3.71 ± 0.03	1.94 ± 0.06	0.33
8601-12705	3.48 ± 0.17	1.00 ± 0.03	1.51 ± 0.04	2.87 ± 0.02	2.54 ± 0.02	1.43 ± 0.06	0.55
8588-9101	3.89 ± 0.11	1.00 ± 0.02	1.20 ± 0.03	2.87 ± 0.01	2.62 ± 0.02	2.63 ± 0.06	0.49
8138-3702	13.32 ± 0.26	1.00 ± 0.05	3.98 ± 0.05	2.87 ± 0.03	3.86 ± 0.01	1.62 ± 0.05	0.74
8138-9101	6.30 ± 0.31	1.00 ± 0.07	2.32 ± 0.08	2.87 ± 0.04	3.04 ± 0.04	1.17 ± 0.05	0.32
8482-3704	10.00 ± 0.13	1.00 ± 0.02	2.03 ± 0.02	2.87 ± 0.01	3.67 ± 0.01	2.38 ± 0.04	0.52
8482-9101	6.56 ± 0.19	1.00 ± 0.05	5.51 ± 0.05	2.87 ± 0.03	4.15 ± 0.02	1.62 ± 0.06	0.51
8554-1902	4.16 ± 0.05	1.00 ± 0.02	3.00 ± 0.02	2.87 ± 0.02	2.70 ± 0.01	1.26 ± 0.06	0.29
8603-12703	1.86 ± 0.06	1.00 ± 0.02	1.14 ± 0.02	2.87 ± 0.02	2.41 ± 0.02	2.30 ± 0.07	0.27
8604-12703	12.39 ± 0.15	1.00 ± 0.03	5.35 ± 0.03	2.87 ± 0.01	5.23 ± 0.02	1.79 ± 0.05	0.48
8604-6102	5.46 ± 0.06	1.00 ± 0.02	2.87 ± 0.02	2.87 ± 0.01	3.91 ± 0.01	1.67 ± 0.05	0.38
8606-3702	8.84 ± 0.12	1.00 ± 0.03	4.00 ± 0.03	2.87 ± 0.02	3.63 ± 0.01	0.93 ± 0.05	0.48

diagram (see Fig. 4). These models are similar to the ones used by Krabbe et al. (2021). A brief description of the input parameters is presented below.

(i) Spectral energy distribution (SED): we considered SED post-AGB star atmosphere models by Rauch (2003) assuming effective temperatures ($T_{\rm eff}$) of 50, 100, and 190 kK, with logarithm of surface gravity $\log(g) = 6$.

(ii) Metallicity: we considered the metallicity of the gas phase ($Z/Z_{\odot}$) equal to 0.2, 0.5, 0.75, 1.0, and 2.0. Assuming the solar oxygen abundance of $12 + \log(O/H)_{\odot} = 8.69$ (Allende Prieto, Lambert & Asplund 2001; Asplund et al. 2009), the corresponding oxygen abundance range is $8.0 \lesssim 12 + \log(O/H) \lesssim 9.2$. All metals were linearly scaled with Z, with the exception of nitrogen, in which we assumed the relation of $\log(N/O) = 1.29 \times [12 + \log(O/H)] - 11.84$ derived by Carvalho et al. (2020) from the abundance estimates of local SFs and Seyfert 2 nuclei.

(iii) Electron density (N_e): we assumed three different electron density values: N_e = 100, 500, and 3000 cm^{-3}, constant along the nebular radius.

(iv) Ionization parameter: this parameter is defined as

$$U = \frac{Q(H)}{4\,\pi\,R_0^2\,n(H)\,c}, \quad (1)$$

where $Q(H)$ (s^{-1}) is the number of hydrogen-ionizing photons emitted by the central ionizing object per second, R_0 (cm) is the distance from the ionization source to the inner surface of the ionized gas cloud, $n(H)$ (cm^{-3}) is the total hydrogen density (ionized, neutral, and molecular), and c ($cm\,s^{-1}$) is the speed of light. We assumed the logarithm of U in the range of $-4.0 \leq \log U \leq -0.5$, with a step of 0.5 dex, which is the same range of values assumed by Krabbe et al. (2021).

CLOUDY is a unidimensional code that assumes a central ionization source, which cannot represent the real situation in gaseous nebulae.

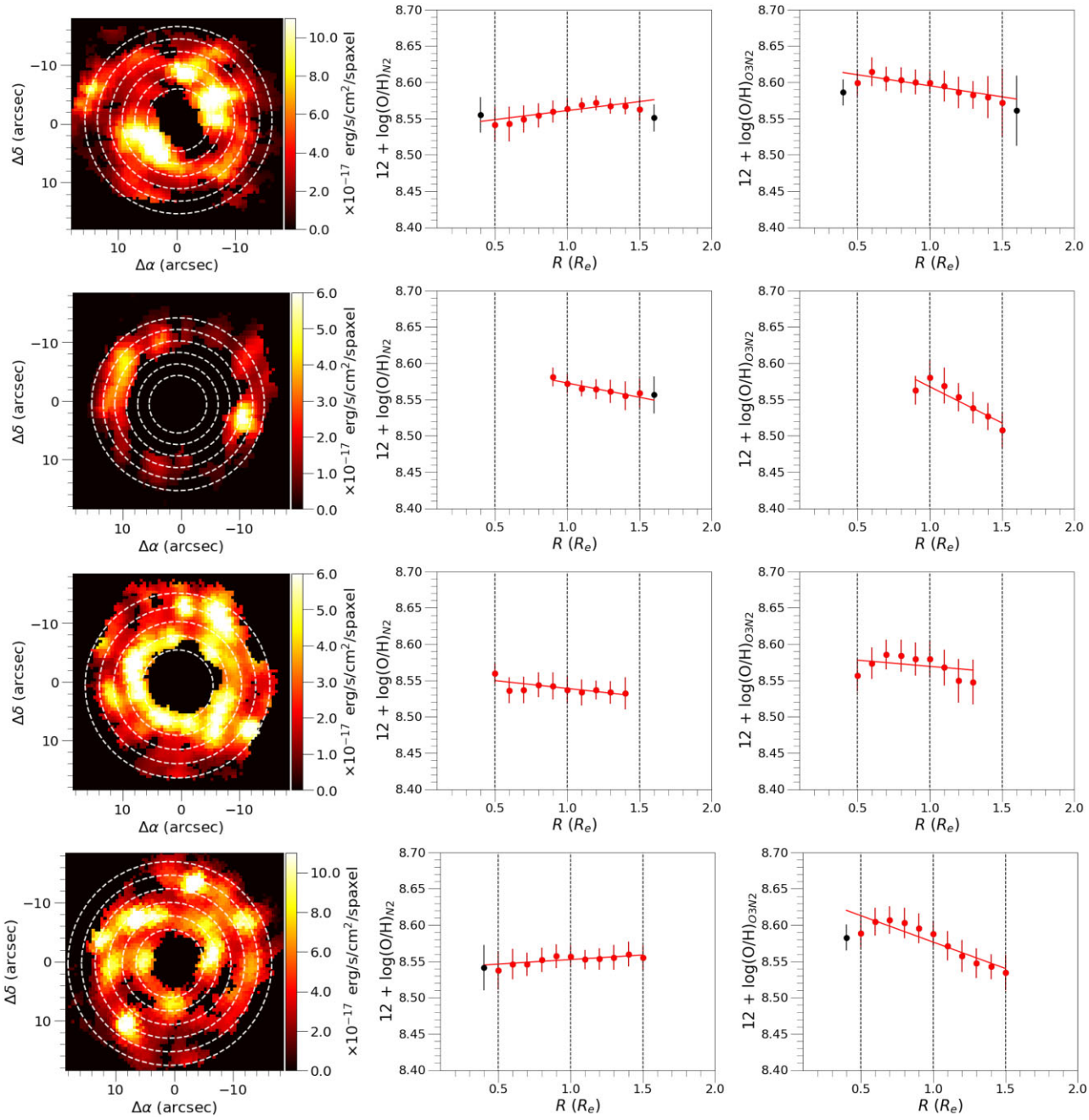

Figure 6. The deprojected Hα maps (left-hand panels) and the metallicity gradients derived using $N2$ and $O3N2$ indices (centre and right-hand panels, respectively) for 7495-12704, 7990-12704, 8249-12704, and 8318-12703 (from top to bottom). The dashed white circles are examples of the radial bins used to compute the metallicity profile from 0.5 and 1.5 R_e, spaced in 0.2 R_e. The red lines are the best fitting between 0.5 and 1.5 R_e and the red open circles are the data points taken into account to fit within this range. The black circles show the data outside this range, which are not considered.

In most cases, a central ionization source cannot genuinely represent the situation, for example, for giant SFs, since the stars may be spread out throughout the region (e.g. Monreal-Ibero et al. 2011). Ercolano, Bastian & Stasińska (2009) and Jamet & Morisset (2008) showed that the distribution of the hot stars (e.g. OB stars) in relation to the gas alters the ionization structure and the electron temperature (also see Jin, Kewley & Sutherland 2022). Hence, the ionization parameter partially depends on the spatial distribution of the ionizing sources with respect to the gas. In our cases, we considered the integrated spectra of the nuclei to try to minimize the stellar distribution effect on the emergent spectra. The assumption of a single star with a representative effective temperature as the main ionizing source, as assumed in our post-AGB models, is a good approximation (see e.g. Zinchenko et al. 2019), since in the case of giant H II regions ionized by stellar clusters (e.g. Mayya & Prabhu 1996; Bosch et al. 2001), the hottest stars dominate the gas ionization (Dors et al. 2017).

Once the photoionization models were built, diagrams of $O3O2 = \log([\mathrm{O\,III}]\,\lambda5007/[\mathrm{O\,II}]\,\lambda3727)$ versus $N2 = \log([\mathrm{N\,II}]\,\lambda6584/\mathrm{H}\alpha)$ and $O3N2 = \log\left(\frac{[\mathrm{O\,III}]\,\lambda5007/\mathrm{H}\beta}{[\mathrm{N\,II}]\,\lambda6583/\mathrm{H}\alpha}\right)$ indices for both the observational data and photoionization model results were obtained. Then, the oxygen abundance (O/H) and the ionization parameter (U) of the

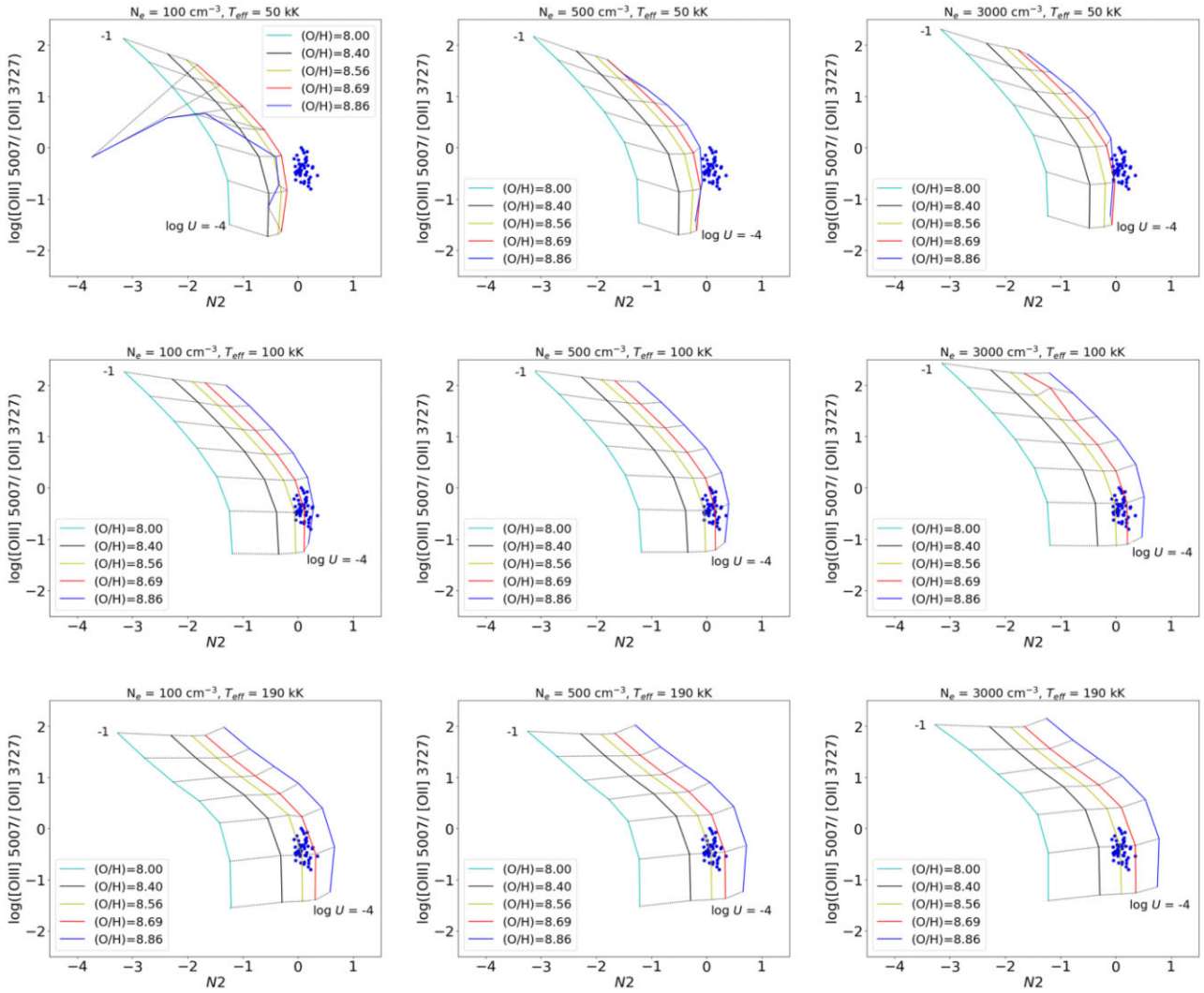

Figure 7. log ([O III] λ5007/[O II] λ3727) versus log ([N II] λ6584/Hα) diagnostic diagram. Coloured solid lines connect the photoionization model results (see Section 3.1) with the same oxygen abundance (O/H) and dotted line models with the same ionization parameter (U), as indicated. The blue point represents the observational line ratios for each nucleus of our sample (see Section 2).

gas phase of each LINER nucleus of the sample were determined by linear interpolation between the model results, which predict the nearest values to the measured emission-line ratios. The methodology applied here is similar to the one adopted by Krabbe et al. (2021).

Note that *O3O2*, *N2*, and *O3N2* indices were selected in this work because the former ratio is sensitive to the ionization degree of the gas phase, while the other two ratios mainly depend on its metallicity. The *N2* index was studied as the metallicity indicator for SFs by Storchi-Bergmann, Calzetti & Kinney (1994) and for Seyfert 2 galaxies by Carvalho et al. (2020). The *O3N2* index was first introduced by Alloin et al. (1979) as a metallicity indicator for SFs, and from there, many calibrations have been proposed in the literature (e.g. Pettini & Pagel 2004; Pérez-Montero & Contini 2009; Marino et al. 2013). The *N2* ratio involves emission lines with close wavelengths, which makes it independent of the reddening correction and the uncertainties on the flux calibration in contrast to the *O3N2* index. Moreover, *N2* involves ions with similar ionization potentials; therefore, it is less dependent on the ionization parameter in comparison to *O3N2*.

3.2 Extrapolating the metallicity gradient

To verify the validity of our calibrations, we compared the oxygen abundance derived from these with measurements obtained from an independent method, which was the extrapolation of the radial oxygen abundance gradient, obtained from H II region estimates along the galaxy disc to the central part of the host galaxies. This indirect method has been widely used in the literature (e.g. Vila-Costas & Edmunds 1992; van Zee et al. 1998; Pilyugin, Vílchez & Contini 2004; Pilyugin, Thuan & Vílchez 2007; Zinchenko et al. 2019; Krabbe et al. 2021; do Nascimento et al. 2022) and produces an independent estimation of the nuclear metallicity.

Due to the random inclination of the galaxies in the sky, the projected galactic discs are ellipticals. The radial profiles are calculated in elliptical annulus, producing some numerical artifacts. For example, the point spread function beam smearing affects the inner radii, creating a spurious flatting of the metallicity gradient at the central regions (e.g. Belfiore et al. 2017), which is worse for higher inclinations. In view of that, we calculate the metallicity gradients between 0.5 and 1.5 R_e, where R_e is the half-light radius of each galaxy, using a radial bin of 0.1 R_e, and only computed the radial

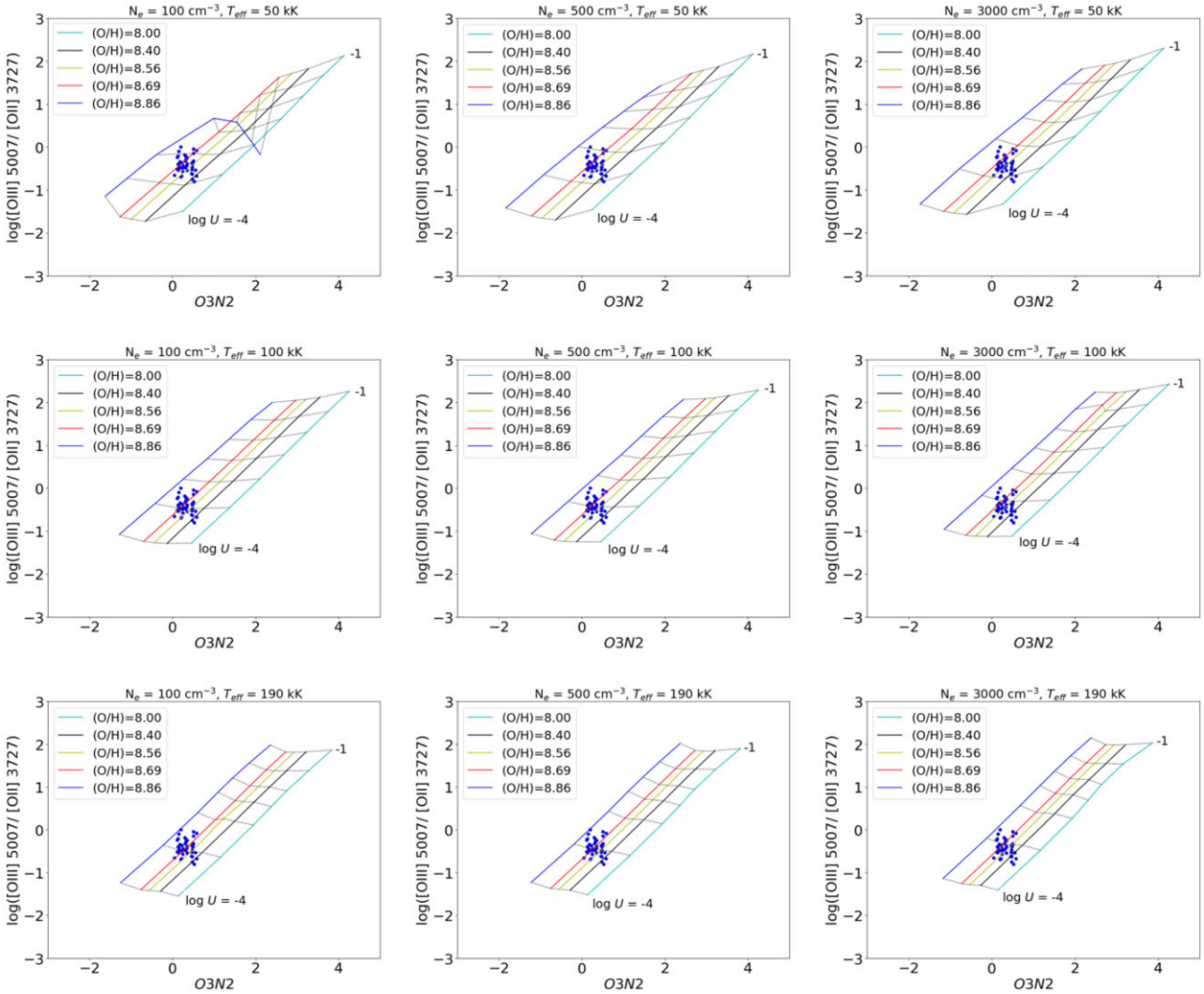

Figure 8. Same as Fig. 7 but considering *O*3*N*2.

bin with at least 20 per cent of the valid spaxels belonging to the corresponding annulus. Another important effect is that the annulus aperture is oversampled along the position angle of the galactic disc, while it is subsampled along the minor axis, yielding biased statistics inside the apertures (e.g. average and median values). To correct this, we applied a novel method introduced by Hernandez-Jimenez (in preparation) to obtain an unbiased metallicity gradient. The key step is to deproject the 2D flux maps before calculating the radial profile. To do this, we followed the recipe used by Elmegreen, Elmegreen & Montenegro (1992), in which the image pixels are stretched along the minor axis by a factor of the inverse cosine of the inclination angle.[6] This operation was performed by using the IRAF IMLINTRAN task. We set the task to preserve the total flux of the image. In the left-hand panels of Fig. 6, we show the deprojected 2D Hα maps for 7495-12704, 7990-12704, 8249-12704, and 8318-12703. In these maps, the central parts are 'removed' because the ionizing sources are not young stars. The elliptical-like SF rings (see Fig. 5) observed in these galaxies are now circular due to the deprojection.

[6]Taken from the manga.drpall table.

Once the 2D emission-line flux maps are deprojected, we built the 2D *O*3*N*2 and *N*2 index maps. Afterwards, we converted them into 2D metallicity abundance maps using the semi-empirical calibrations of these indices proposed for SFs by Marino et al. (2013). These authors performed these calibrations using observations of 3423 H II regions from the Calar Alto Legacy Integral Field Area Survey (CALIFA) survey based on the T_e method. The *O*3*N*2 and *N*2 calibrations are, respectively, given by

$$12 + \log(\mathrm{O/H}) = 8.533(\pm0.012) - 0.214(\pm0.012) \times O3N2 \quad (2)$$

and

$$12 + \log(\mathrm{O/H}) = 8.743(\pm0.027) + 0.462(\pm0.024) \times N2, \quad (3)$$

which are valid in the $-1.1 < O3N2 < 1.7$ range for equation (2) and in the $-1.6 < N2 < -0.2$ range for equation (3). Finally, we calculate the radial profile from Hα flux-weighted median value of the abundance map along the circular annuli. Then, the following linear fitting was obtained:

$$12 + \log(\mathrm{O/H}) = 12 + \log(\mathrm{O/H})_0 + (\mathrm{grad} \times R/R_e), \quad (4)$$

where $12 + \log(\mathrm{O/H})$ is the oxygen abundance at a given galactocentric distance R (in units of arcsec), grad is the regression slope, and

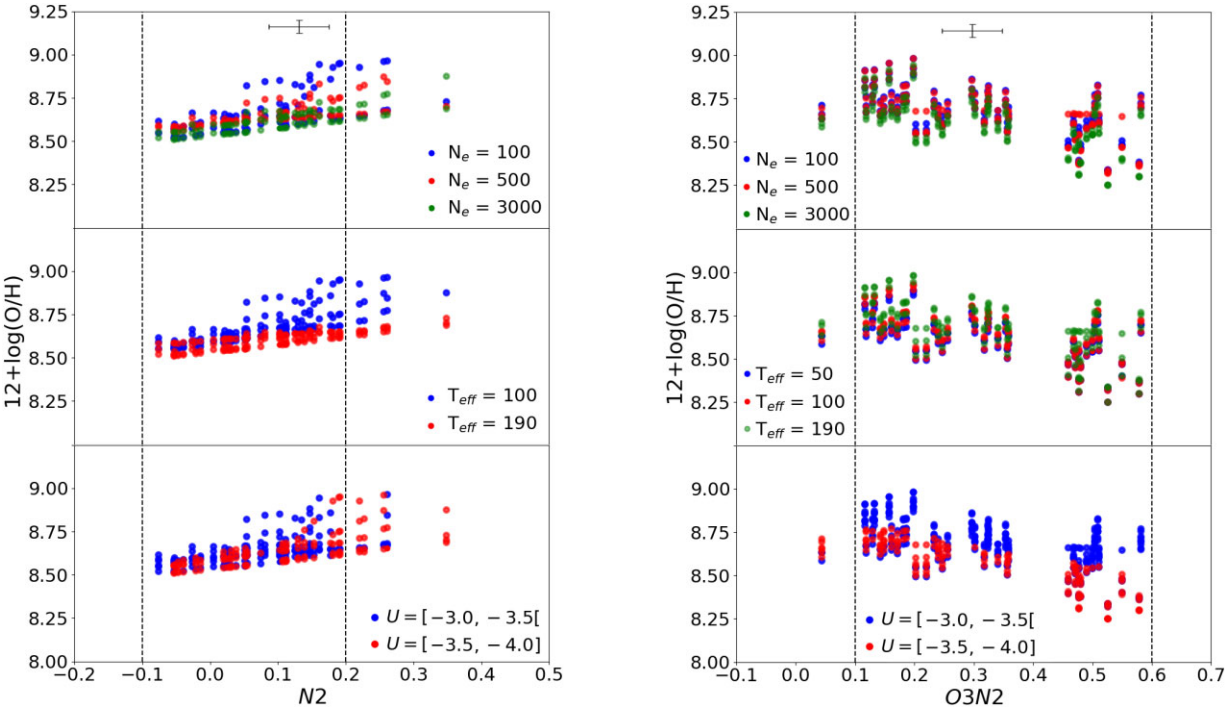

Figure 9. Left-hand column: oxygen abundance versus the *N*2 index. Oxygen abundances were estimated interpolating the results from the models. Different colours are used to differentiate the estimated properties for the objects in our sample considering different N_e (upper panel), T_{eff} (middle panel), and log (U) (bottom panel) values as indicated. Right-hand column: same as the left-hand column but for *O3N2*. Error bars in each panel represent the typical 0.1 dex error in the observational measurements of the *N*2 and *O3N2* indices and the average error of 0.10 and 0.12 dex in the interpolated values, considering *N*2 and *O3N2*, respectively. The grey vertical lines correspond to the limits of the $-0.1 < N2 < 0.2$ and $0.1 < O3N2 < 0.6$ ranges, which correspond to the bulk of the observational data.

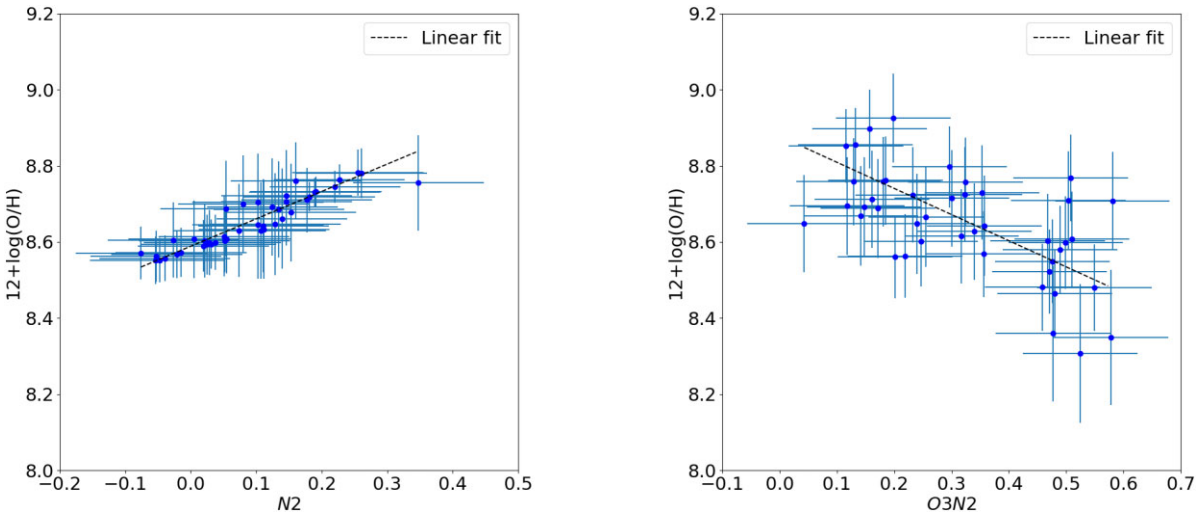

Figure 10. Left-hand panel: oxygen abundances versus the *N*2 index. Points represent the average estimations from the photoionization model results with errors. Right-hand panel: Same as the left-hand panel but for oxygen abundance versus *O3N2* index. Black line represents the linear fit given by equations (5) and (6) applying the ODR method, i.e. considering the errors, whose correlation coefficients are $R = 0.85$ and 0.37, respectively.

$12 + \log(O/H)_0$ is the extrapolated value of the metallicity gradient at the centre of the galaxy ($R = 0$ kpc). This fitting was performed for both *N*2 and *O3N2* indices obtaining two pairs of $12 + \log(O/H)_0$ and grad for each galaxy. We computed these metallicity gradients for galaxies with at least five radial bins between 0.5 and 1.5 R_e. In this way, we were able to perform the radial fitting for 33 and 32 galaxies using the *N*2 and *O3N2* indices, respectively. The central and right-hand panels of Fig. 6 present for 7495-12704, 7990-12704, 8249-12704, and 8318-12703 the metallicity gradients derived from *N*2 and *O3N2* indices, respectively.

4 RESULTS

The diagnostic diagrams containing the photoionization model results and the observational data of the nuclei for the objects of our sample are shown in Figs 7 and 8, for log([O III] λ5007/[O II] λ3727)

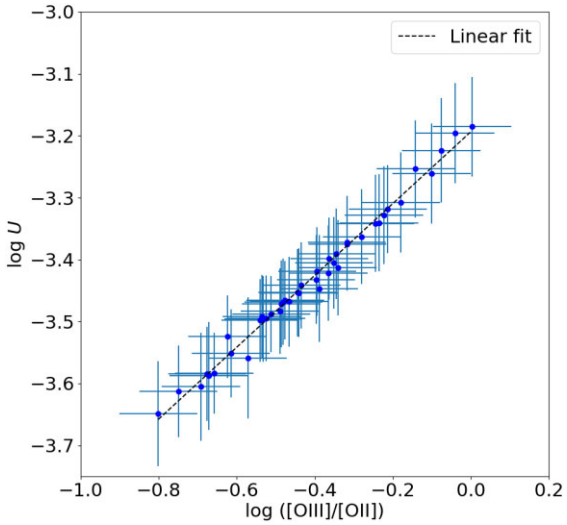

Figure 11. Same as Fig. 7, but for log U versus log([O III] λ5007/[O II] λ3727. Line represents the linear fitting (equation 7) whose correlation coefficient is $R = 0.98$.

versus $N2$ index and log([O III] λ5007/[O II] λ3727) versus the $O3N2$ indices, respectively. Nine model grids with different N_e and T_{eff} values are considered for the $N2$ and $O3N2$ indices. For models with 100 and 190 kK, all observational data fall within the regions occupied by the models, while models with $T_{eff} = 50$ kK do not reproduce well the emission-line ratios for the $N2$ index. This result agrees with that found by Krabbe et al. (2021) for UGC 4805. Thus, the photoionization model results with $T_{eff} = 50$ kK for the $N2$ index were not taken into account in our study. The values of O/H and U were derived using linear interpolations between the photoionization models following the procedure applied by Krabbe et al. (2021). In this way, we derived three pairs of points for each object: ($N2$, O/H), ($O3N2$, O/H), and ($O3O2$, log U). Then, we obtained a set of point pairs for the sample and analysed the building of the calibrations.

That allowed us to analyse the dependence of the oxygen abundance on N_e, T_{eff}, and log (U) as a function of the $N2$ and $O3N2$ indices, which are shown in Fig. 9. Data exhibited in this figure correspond to the interpolated model values obtained from Figs 7 and 8 for each object, i.e. each galaxy has six points in each left-hand panel of Fig. 9 and nine points in each right-hand panel of Fig. 9. We limited the analysis to the ranges of $-0.1 < N2 < 0.2$ and $0.1 < O3N2 < 0.6$, which correspond to the bulk of the observational data. For the $N2$ index (left-hand panels of Fig. 9), the higher oxygen abundance values were derived from lower values of T_{eff} and N_e, without dependence on log U. On the other hand, for the $O3N2$ index, the oxygen abundance is dependent on the N_e, T_{eff}, and log U, in that the higher oxygen abundance was derived from the lower values of density and higher values of effective temperature and ionization parameter. However, as seen in Fig. 9, the average error in the observational values of $N2$ and $O3N2$ produces uncertainties in the abundance estimations of the order of or even larger than those due to the variation of the nebular parameters (see also Carvalho et al. 2020).

Therefore, using the orthogonal distance regression (ODR) method, which takes into account errors in both the x and y variables (Boggs & Rogers 1990), we performed two unidimensional semi-empirical calibration considering all points, i.e. for each galaxy, the assumed oxygen abundance value is the average of the interpolations for the six photoionization grid models from Fig. 7 and the nine photoionization grid models from Fig. 8. Fig. 10 presents the averaged oxygen abundance values versus the $N2$ and $O3N2$ indices (left- and right-hand panels, respectively). The $N2$ index is well correlated with the oxygen abundance with low dispersion, while the $O3N2$ index also has a linear correlation with the oxygen abundance, but with a higher dispersion. The derived linear calibrations are given by

$$12 + \log(\mathrm{O/H}) = 0.71(\pm0.03)N2 + 8.58(\pm0.01) \quad (5)$$

and

$$12 + \log(\mathrm{O/H}) = -0.68(\pm0.11)O3N2 + 8.87(\pm0.03). \quad (6)$$

The interpolated values from Figs 7 and 8 can also be used to derive a calibration between the observed log([O III] λ5007/[O II] λ3727) and the ionization parameter U, which is assumed as the average, for each object, of the interpolated model values. Fig. 11 contains these values, together with the obtained linear regression fit given by

$$\log U = 0.57(\pm0.01)\, x - 3.19(\pm0.01), \quad (7)$$

where x = log([O III] λ5007/[O II] λ3727). We did not find any dependence of this relation on N_e, T_{eff}, and O/H, similar to the results obtained by Carvalho et al. (2020) for NLRs of Seyfert 2 galaxies.

5 DISCUSSIONS

In the chemical abundance determinations of the gas phase, the knowledge of the ionizing source is fundamental, especially when it is estimated using indirect methods. The nature of the ionizing source of LINERs is an open problem in astronomy, and three mechanisms have been proposed as responsible for the ionization: shocks (Heckman 1980), accretion gas into a central black hole (AGN; Ferland & Netzer 1983; Halpern & Steiner 1983; Ho et al. 1993), and hot stars (post-AGB stars; Terlevich & Melnick 1985; Shields 1992; Taniguchi et al. 2000). In our specific case, the sample is composed of objects with a LINER nucleus, and according to the WHAN diagram are classified as RGs.

We argued that the LINER ionization sources of these galaxies are probably post-AGB stars spread along the gas (see also Krabbe et al. 2021). Therefore, based on this assumption, we proposed two semi-empirical calibrations between the $N2$ and $O3N2$ line ratios and the metallicity, as well as a calibration between [O III]/[O II] ratio and the ionization parameter U derived from photoionization models assuming the ionizing sources are post-AGBs.

In Table 3, we list for all sampled galaxies the oxygen abundance values obtained using the calibrations proposed in this work (see Section 4) and those derived by extrapolating the radial gradients $12 + \log(\mathrm{O/H})_0$ (see Section 3.2), as well as the ionization parameter values obtained by using equation (7). Fig. 12 shows $12 + \log(\mathrm{O/H})_0$ versus $12 + \log(\mathrm{O/H})$ through the $N2$ index (left-hand panel) and those through the $O3N2$ index (right-hand panel). Both $12 + \log(\mathrm{O/H}) - N2$ and $12 + \log(\mathrm{O/H}) - O3N2$ relations produced higher oxygen abundance values than those derived by the oxygen abundance gradient extrapolation method. Taking into account the observational uncertainties (∼0.1 dex; Kennicutt, Bresolin & Garnett 2003) and the accuracy of the theoretical and (semi-)empirical calibrations (∼0.1 dex; e.g. Kewley & Dopita 2002; Carvalho et al. 2020; Dors 2021), we can claim that the present estimated abundances through the different methods agree with each other. Therefore, these estimations support the validity of the semi-empirical calibration for LINER objects obtained in this work. Using these calibrations, we found that LINERs exhibit an oxygen abundance range $8.48 \lesssim 12 + \log(\mathrm{O/H}) \lesssim 8.84$, with a

Table 3. Oxygen abundance values obtained through the *N*2 and *O*3*N*2 calibrations presented in equations (5) and (6), and the mean values of the ionization parameter obtained through equation (7). Extrapolated radial oxygen abundance values, $12 + \log(O/H)_0$, estimated from both *N*2 and *O*3*N*2 indices (see Section 3.2) are also shown.

Plate-IFU	$12 + \log(O/H)$		$\langle \log U \rangle$	$12 + \log(O/H)_0$	
	*N*2	*O*3*N*2		*N*2	*O*3*N*2
7495-12704	8.62 ± 0.02	8.74 ± 0.05	−3.19 ± 0.01	8.54 ± 0.02	8.63 ± 0.02
7977-3704	8.57 ± 0.01	8.71 ± 0.06	−3.47 ± 0.02	8.61 ± 0.02	8.56 ± 0.03
7977-12703	8.54 ± 0.00	8.75 ± 0.05	−3.46 ± 0.01	8.60 ± 0.01	8.58 ± 0.02
7990-6103	8.55 ± 0.01	8.54 ± 0.08	−3.55 ± 0.02	8.61 ± 0.02	8.60 ± 0.03
7990-12704	8.59 ± 0.01	8.67 ± 0.06	−3.37 ± 0.01	8.61 ± 0.03	8.67 ± 0.05
8083-12704	8.58 ± 0.01	8.79 ± 0.04	−3.32 ± 0.01	8.56 ± 0.02	8.72 ± 0.03
8131-9102	8.71 ± 0.06	8.55 ± 0.08	−3.62 ± 0.02	8.58 ± 0.04	8.56 ± 0.09
8140-12703	8.62 ± 0.02	8.72 ± 0.05	−3.57 ± 0.02	8.56 ± 0.02	8.62 ± 0.02
8243-9102	8.83 ± 0.12	8.77 ± 0.05	−3.50 ± 0.02	–	–
8243-12701	8.69 ± 0.04	8.55 ± 0.08	−3.46 ± 0.01	8.57 ± 0.02	8.62 ± 0.02
8247-3701	8.60 ± 0.02	8.78 ± 0.04	−3.42 ± 0.01	8.61 ± 0.02	8.61 ± 0.05
8249-12704	8.64 ± 0.03	8.52 ± 0.09	−3.21 ± 0.01	8.56 ± 0.02	8.59 ± 0.03
8252-12702	8.71 ± 0.02	8.48 ± 0.09	−3.58 ± 0.01	–	–
8254-3704	8.62 ± 0.01	8.70 ± 0.06	−3.44 ± 0.01	8.54 ± 0.02	8.59 ± 0.02
8257-1902	8.57 ± 0.01	8.76 ± 0.05	−3.44 ± 0.02	8.62 ± 0.03	8.60 ± 0.04
8258-12704	8.74 ± 0.05	8.51 ± 0.09	−3.65 ± 0.01	8.60 ± 0.04	8.54 ± 0.06
8259-9102	8.60 ± 0.04	8.63 ± 0.07	−3.50 ± 0.01	8.54 ± 0.02	8.61 ± 0.02
8313-9102	8.71 ± 0.04	8.74 ± 0.05	−3.38 ± 0.01	8.61 ± 0.01	8.64 ± 0.03
8313-12705	8.68 ± 0.04	8.63 ± 0.07	−3.33 ± 0.01	8.61 ± 0.02	8.58 ± 0.05
8318-12703	8.68 ± 0.06	8.67 ± 0.06	−3.29 ± 0.02	8.54 ± 0.02	8.65 ± 0.02
8320-9102	8.67 ± 0.03	8.65 ± 0.07	−3.32 ± 0.01	8.58 ± 0.02	8.62 ± 0.03
8332-12705	8.72 ± 0.02	8.56 ± 0.08	−3.54 ± 0.01	8.58 ± 0.02	8.62 ± 0.03
8330-9102	8.65 ± 0.02	8.76 ± 0.05	−3.25 ± 0.01	–	–
8332-6103	8.63 ± 0.01	8.52 ± 0.09	−3.37 ± 0.02	8.57 ± 0.02	8.57 ± 0.04
8440-12704	8.62 ± 0.08	8.75 ± 0.05	−3.39 ± 0.01	8.59 ± 0.01	8.49 ± 0.06
8481-1902	8.59 ± 0.04	8.65 ± 0.06	−3.46 ± 0.02	–	–
8482-12703	8.76 ± 0.02	8.63 ± 0.07	−3.41 ± 0.02	8.59 ± 0.02	8.67 ± 0.03
8549-3703	8.68 ± 0.07	8.50 ± 0.09	−3.49 ± 0.02	8.60 ± 0.01	8.57 ± 0.02
8550-6103	8.61 ± 0.03	8.77 ± 0.05	−3.47 ± 0.01	8.56 ± 0.01	8.63 ± 0.02
8550-12704	8.74 ± 0.03	8.70 ± 0.06	−3.52 ± 0.02	8.56 ± 0.02	8.66 ± 0.04
8550-12705	8.66 ± 0.00	8.54 ± 0.08	−3.41 ± 0.01	8.57 ± 0.03	8.60 ± 0.05
8552-9101	8.66 ± 0.01	8.84 ± 0.03	−3.56 ± 0.02	8.59 ± 0.02	8.59 ± 0.02
8601-12705	8.54 ± 0.04	8.71 ± 0.06	−3.40 ± 0.01	8.55 ± 0.02	8.59 ± 0.03
8588-9101	8.55 ± 0.01	8.79 ± 0.04	−3.48 ± 0.01	8.60 ± 0.01	8.59 ± 0.02
8138-3702	8.67 ± 0.03	8.55 ± 0.08	−3.49 ± 0.02	–	–
8138-9101	8.60 ± 0.01	8.64 ± 0.07	−3.44 ± 0.01	8.58 ± 0.02	8.64 ± 0.02
8482-3704	8.66 ± 0.00	8.73 ± 0.05	−3.58 ± 0.01	8.58 ± 0.02	8.62 ± 0.03
8482-9101	8.69 ± 0.08	8.48 ± 0.09	−3.23 ± 0.01	8.53 ± 0.06	–
8554-1902	8.56 ± 0.04	8.53 ± 0.09	−3.27 ± 0.01	–	–
8603-12703	8.53 ± 0.03	8.78 ± 0.04	−3.31 ± 0.01	–	–
8604-12703	8.76 ± 0.04	8.55 ± 0.08	−3.40 ± 0.01	–	–
8604-6102	8.68 ± 0.03	8.65 ± 0.07	−3.35 ± 0.02	–	–
8606-3702	8.65 ± 0.03	8.53 ± 0.08	−3.39 ± 0.01	–	–

mean value of $12 + \log(O/H) = 8.65$. Fig. 13 contains a comparison between the abundance values obtained using our two calibrations. *N*2 and *O*3*N*2 oxygen abundance estimations are in agreement. However, this relation has a high dispersion, and the difference between both estimations (upper panel) exhibits a systematic linear behaviour. Therefore, considering these results and that the *O*3*N*2 calibration presents a higher dispersion than the *N*2 (see Fig. 10), even if we are able to use both calibrations to estimate the central oxygen abundance of LINER galaxies, we recommend using the *N*2 calibration.

For the ionization parameter, it is well known that LINERs have a lower ionization parameter than Seyferts (see Ferland & Netzer 1983; Kewley et al. 2006). Fig. 14 compares the estimated values of the logarithm of the ionization parameter ($\log U$) of our sample of LINERs with those derived for a sample of Seyfert 2 galaxies studied by Carvalho et al. (2020). The values of $\log U$ are in the range from −4 to −2.0 and from −3.6 to −3.2, for the Seyfert 2 and LINERs, respectively. The mean value of $\log U$ is about −3.21 ($\sigma = 0.45$) and −3.42 ($\sigma = 0.11$), for the Seyfert 2 and LINER galaxies, respectively. This difference represents a factor of almost 2 on a linear scale. Hence, although some Seyfert 2 galaxies have lower ionization parameters, they extend to much higher values than the ones estimated for the LINERs. This large variation in $\log U$ was also reported by Stasińska (1984) for Seyfert nuclei. This author presented a series of diagrams in which different line intensity ratios are plotted for a sample of Seyfert 2 galaxies and found that objects with low-density clouds ($< 10^4 cm^3$) present $\log U$ that varies from −4 to −2.

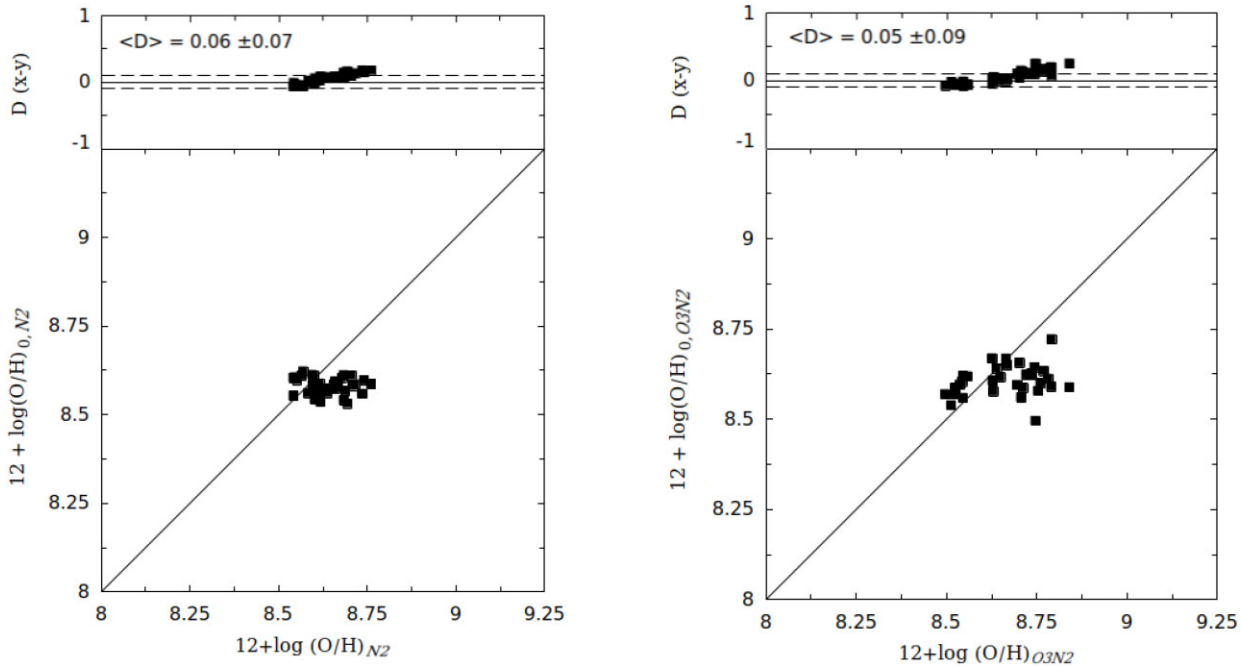

Figure 12. Bottom left-hand panel: comparison between $12 + \log(O/H)$ obtained using the calibration $12 + \log(O/H) - N2$ proposed in this work and the one obtained through the extrapolation of the radial gradient (see Section 3.2). Top left-hand panel: difference $\langle D \rangle$ between the metallicity estimations based on our $12 + \log(O/H) - N2$ relation and the one obtained through the extrapolation using the $N2$ index. The average difference between these estimations is provided. Dashed lines indicate the uncertainty of ±0.1 dex assumed in $12 + \log(O/H)$ estimations via strong emission-line methods (Kewley et al. 2001). Right-hand panels: the same as the left-hand panels but using the $O3N2$ index.

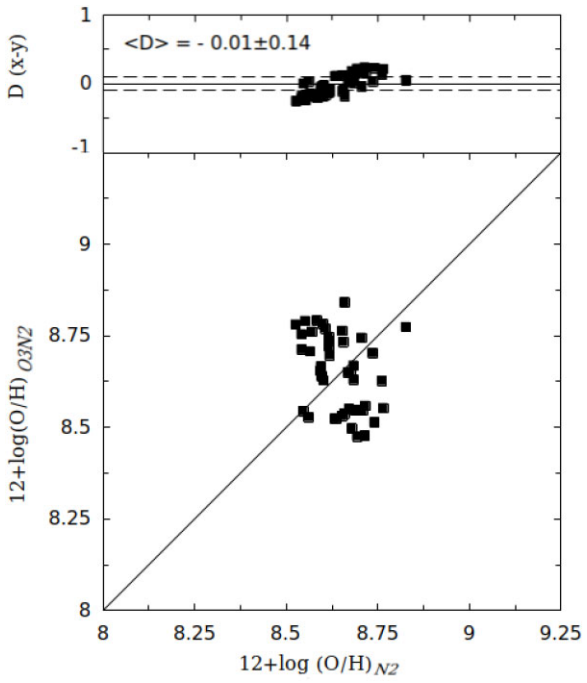

Figure 13. Bottom panel: oxygen abundance estimations derived through our $O3N2$ calibration (equation 6) plotted against the ones estimated through the $N2$ calibration (equation 5). Solid line represents the equality between these oxygen estimations. Top panel: difference $\langle D \rangle$ between both estimations. The average difference is indicated.

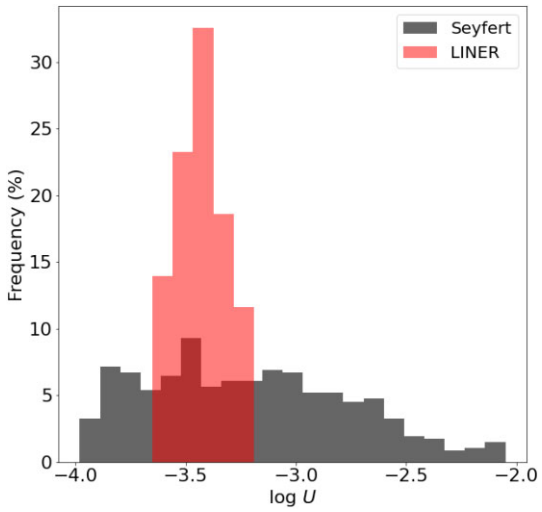

Figure 14. Histogram containing the logarithm of the ionization parameters of our objects derived through equation (7) and the values derived for a sample of Seyfert 2 galaxies studied by Carvalho et al. (2020).

6 CONCLUSION

Using optical data of 43 LINER galaxies obtained from the MaNGA survey, we proposed, for the first time, two semi-empirical calibrations based on photoionization models to estimate the oxygen abundance of this class of objects, as a function of the $N2$ and $O3N2$ emission-line intensity ratios. Due to the nuclei of the objects in our sample classified as RGs according to the WHAN diagnostic diagram, we argue that these LINERs are probably ionized by post-AGB stars. Therefore, to derive the calibrations, we built

photoionization models using the CLOUDY code considering post-AGB stars with three different effective temperatures (50, 100, and 190 kK) as the ionizing sources. Using the calibrations proposed in this work, we found that LINERs exhibit an oxygen abundance range $8.48 \lesssim 12 + \log(\mathrm{O/H}) \lesssim 8.84$, with a mean value of $12 + \log(\mathrm{O/H}) = 8.65$. We compared the results produced by both calibrations and found that they are in agreement. Comparing the results produced by the calibrations, taking into account the observational and theoretical errors, we found good agreement. Considering this result and that the $12 + \log(\mathrm{O/H}) - N2$ calibration presents a much smaller dispersion than the $12 + \log(\mathrm{O/H}) - O3N2$ calibration, we recommend the use of the $N2$ index to estimate the oxygen abundances of LINERs. We compared the metallicities produced by the proposed calibrations, with those derived by extrapolating the disc oxygen abundance gradients to the centre of the galaxies, finding that they are in good agreement. We also derived a calibration between the logarithm of the ionization parameter and the [O III]/[O II] emission-line ratio.

ACKNOWLEDGEMENTS

CBO is grateful to the Fundação de Amparo à Pesquisa do Estado de São Paulo (FAPESP) for the support under grant 2019/11934-0 and to the Coordenação de Aperfeiçoamento de Pessoal de Nível Superior (CAPES). ACK thanks FAPESP for the support grant 2020/16416-5 and the Conselho Nacional de Desenvolvimento Científico e Tecnológico (CNPq). JAHJ acknowledges support from FAPESP, process number 2021/08920-8. OLD is grateful to FAPESP and CNPq. IAZ acknowledges support by the National Academy of Sciences of Ukraine under the Research Laboratory Grant for young scientists No. 0120U100148. AFM gratefully acknowledges support from CAPES.

Software: ASTROPLOTLIB (Hernandez-Jimenez 2022; Hernandez-Jimenez et al. 2013, 2015), ASTROPY (Astropy Collaboration 2013, 2018), SCIPY (Virtanen et al. 2020), NUMPY (Harris et al. 2020), and MATPLOTLIB (Hunter 2007).

DATA AVAILABILITY

The data underlying this paper will be shared on reasonable request to the corresponding author.

REFERENCES

Aguado D. S. et al., 2019, ApJS, 240, 23
Allende Prieto C., Lambert D. L., Asplund M., 2001, ApJ, 556, L63
Alloin D., Collin-Souffrin S., Joly M., Vigroux L., 1979, A&A, 78, 200
Alloin D., Bica E., Bonatto C., Prugniel P., 1992, A&A, 266, 117
Asplund M., Grevesse N., Sauval A. J., Scott P., 2009, ARA&A, 47, 481
Astropy Collaboration, 2013, A&A, 558, A33
Astropy Collaboration, 2018, AJ, 156, 123
Baldwin J. A., Phillips M. M., Terlevich R., 1981, PASP, 93, 5
Belfiore F. et al., 2017, MNRAS, 469, 151
Belfiore F. et al., 2019, AJ, 158, 160
Blanton M. R. et al., 2017, AJ, 154, 28
Boggs P. T., Rogers J. E., 1990, in Brown P. J., Wayne A. F., eds, Contemporary Mathematics: Orthogonal distance regression, Vol. 112. Providence, USA, p. 186
Bosch G., Selman F., Melnick J., Terlevich R., 2001, A&A, 380, 137
Bremer M., Scharwächter J., Eckart A., Valencia-S. M., Zuther J., Combes F., Garcia-Burillo S., Fischer S., 2013, A&A, 558, A34
Bundy K. et al., 2015, ApJ, 798, 7
Cappellari M., 2017, MNRAS, 466, 798
Cappellari M., Copin Y., 2003, MNRAS, 342, 345
Cardelli J. A., Clayton G. C., Mathis J. S., 1989, ApJ, 345, 245
Carvalho S. P. et al., 2020, MNRAS, 492, 5675
Castro C. S., Dors O. L., Cardaci M. V., Hägele G. F., 2017, MNRAS, 467, 1507
Cid Fernandes R., Stasińska G., Schlickmann M. S., Mateus A., Vale Asari N., Schoenell W., Sodré L., 2010, MNRAS, 403, 1036
Cid Fernandes R., Stasińska G., Mateus A., Vale Asari N., 2011, MNRAS, 413, 1687
Díaz Á. I., Terlevich E., Castellanos M., Hägele G. F., 2007, MNRAS, 382, 251
do Nascimento J. C. et al., 2022, MNRAS, 513, 807
Dors O. L., 2021, MNRAS, 507, 466
Dors O. L. J., Storchi-Bergmann T., Riffel R. A., Schimdt A. A., 2008, A&A, 482, 59
Dors O. L., Cardaci M. V., Hägele G. F., Rodrigues I., Grebel E. K., Pilyugin L. S., Freitas-Lemes P., Krabbe A. C., 2015, MNRAS, 453, 4102
Dors O. L., Hägele G. F., Cardaci M. V., Krabbe A. C., 2017, MNRAS, 466, 726
Dors O. L. et al., 2020, MNRAS, 492, 468
Drory N. et al., 2015, AJ, 149, 77
Elmegreen B. G., Elmegreen D. M., Montenegro L., 1992, ApJS, 79, 37
Ercolano B., Bastian N., Stasińska G., 2009, Ap&SS, 324, 199
Falcón-Barroso J., Sánchez-Blázquez P., Vazdekis A., Ricciardelli E., Cardiel N., Cenarro A. J., Gorgas J., Peletier R. F., 2011, A&A, 532, A95
Ferland G. J., Netzer H., 1983, ApJ, 264, 105
Ferland G. J. et al., 2017, Rev. Mex. Astron. Astrofis., 53, 385
Hägele G. F., Pérez-Montero E., Díaz Á. I., Terlevich E., Terlevich R., 2006, MNRAS, 372, 293
Hägele G. F., Díaz Á. I., Terlevich E., Terlevich R., Pérez-Montero E., Cardaci M. V., 2008, MNRAS, 383, 209
Halpern J. P., Steiner J. E., 1983, ApJ, 269, L37
Harris C. R. et al., 2020, Nature, 585, 357
Heckman T. M., 1980, A&A, 87, 152
Hernandez-Jimenez J. A., 2022, Astrophysics Source Code Library, record ascl:2204.002
Hernandez-Jimenez J. A., Pastoriza M. G., Rodrigues I., Krabbe A. C., Winge C., Bonatto C., 2013, MNRAS, 435, 3342
Hernandez-Jimenez J. A., Pastoriza M. G., Bonatto C., Rodrigues I., Krabbe A. C., Winge C., 2015, MNRAS, 451, 2278
Ho L. C., Filippenko A. V., Sargent W. L. W., 1993, ApJ, 417, 63
Hunter J. D., 2007, Comput. Sci. Eng., 9, 90
Izotov Y. I., Thuan T. X., 2008, ApJ, 687, 133
Jamet L., Morisset C., 2008, A&A, 482, 209
Jensen E. B., Strom K. M., Strom S. E., 1976, ApJ, 209, 748
Jin Y., Kewley L. J., Sutherland R., 2022, ApJ, 927, 37
Kauffmann G. et al., 2003, MNRAS, 346, 1055
Kennicutt Robert C. J., Bresolin F., Garnett D. R., 2003, ApJ, 591, 801
Kewley L. J., Dopita M. A., 2002, ApJS, 142, 35
Kewley L. J., Dopita M. A., Sutherland R. S., Heisler C. A., Trevena J., 2001, ApJ, 556, 121
Kewley L. J., Groves B., Kauffmann G., Heckman T., 2006, MNRAS, 372, 961
Kewley L. J., Nicholls D. C., Sutherland R. S., 2019, ARA&A, 57, 511
Krabbe A. C., Oliveira C. B., Zinchenko I. A., Hernández-Jiménez J. A., Dors O. L., Hägele G. F., Cardaci M. V., Telles N. R., 2021, MNRAS, 505, 2087
López-Sánchez Á. R., Esteban C., 2010, A&A, 517, A85
Maiolino R., Mannucci F., 2019, A&AR, 27, 3
Marino R. A. et al., 2013, A&A, 559, A114
Mayya Y. D., Prabhu T. P., 1996, AJ, 111, 1252
Monreal-Ibero A., Relaño M., Kehrig C., Pérez-Montero E., Vílchez J. M., Kelz A., Roth M. M., Streicher O., 2011, MNRAS, 413, 2242
Netzer H., 2013, The Physics and Evolution of Active Galactic Nuclei. Cambridge Univ. Press, Cambridge
Osterbrock D. E., Ferland G. J., 2006, Astrophysics of Gaseous Nebulae and Active Galactic Nuclei. University Science Books, Sausalito, California

Pagel B. E. J., Edmunds M. G., Blackwell D. E., Chun M. S., Smith G., 1979, MNRAS, 189, 95
Peimbert M., Peimbert A., Delgado-Inglada G., 2017, PASP, 129, 082001
Pérez-Montero E., 2017, PASP, 129, 043001
Pérez-Montero E., Contini T., 2009, MNRAS, 398, 949
Pettini M., Pagel B. E. J., 2004, MNRAS, 348, L59
Pilyugin L. S., 2003, A&A, 399, 1003
Pilyugin L. S., Vílchez J. M., Contini T., 2004, A&A, 425, 849
Pilyugin L. S., Thuan T. X., Vílchez J. M., 2007, MNRAS, 376, 353
Rauch T., 2003, A&A, 403, 709
Sánchez S. F. et al., 2016, Rev. Mex. Astron. Astrofis., 52, 171
Sánchez-Blázquez P. et al., 2006, MNRAS, 371, 703
Shields J. C., 1992, ApJ, 399, L27
Singh R. et al., 2013, A&A, 558, A43
Smee S. A. et al., 2013, AJ, 146, 32
Stasińska G., 1984, A&A, 135, 341
Storchi-Bergmann T., Calzetti D., Kinney A. L., 1994, ApJ, 429, 572
Storchi-Bergmann T., Schmitt H. R., Calzetti D., Kinney A. L., 1998, AJ, 115, 909
Taniguchi Y., Shioya Y., Murayama T., 2000, AJ, 120, 1265
Terlevich R., Melnick J., 1985, MNRAS, 213, 841
Toribio San Cipriano L., Domínguez-Guzmán G., Esteban C., García-Rojas J., Mesa-Delgado A., Bresolin F., Rodríguez M., Simón-Díaz S., 2017, MNRAS, 467, 3759
van Zee L., Salzer J. J., Haynes M. P., O'Donoghue A. A., Balonek T. J., 1998, AJ, 116, 2805
Vila-Costas M. B., Edmunds M. G., 1992, MNRAS, 259, 121
Virtanen P. et al., 2020, Nat. Methods, 17, 261
Wake D. A. et al., 2017, AJ, 154, 86
Westfall K. B. et al., 2019, AJ, 158, 231
Yan R., 2018, MNRAS, 481, 476
Yan R., Blanton M. R., 2012, ApJ, 747, 61
Zinchenko I. A., Dors O. L., Hägele G. F., Cardaci M. V., Krabbe A. C., 2019, MNRAS, 483, 1901

This paper has been typeset from a TEX/LATEX file prepared by the author.